Spin-torch experiment on reaction centers of Rhodobacter sphaeroides

Sai Sankar Gupta, K.B.

Chapter 1

General introduction

1.1 Bacterial reaction center

1.1.1 Photosynthesis

Life on Earth is predominantly due to photosynthesis, a process which consists of two different pathways namely anoxygenic and oxygenic. In anoxygenic photosynthesis only carbon dioxide is consumed, while in oxygenic photosynthesis along with that oxygen is also liberated. In general photosynthetic process produces food for living beings and provides the fossil fuels for human energy consumption. Photosynthesis has been well studied in higher plants, algae, cyanobacteria as well as in green and purple bacteria (Blankenship, 2002). These organisms utilize sunlight to power their cellular processes and derive their biomass through chemical reactions driven by light. Photosynthesis is initiated by photon absorption in an antenna pigment. A wide variety of different antenna complexes are found in different photosynthetic systems (Blankenship, 2002) using pigments such as (bacterio)chlorophylls (B)Chl, carotenoids and bilins (*i.e.*, open-chain tetrapyrroles). Antennas allow to increase the spectral range of the photons as well as the absorption cross section without having to build an entire reaction center. Due to the functional organisation of the antenna, excitations are transferred into the photosynthetic reaction center (RC) in which the charge separation occurs. The RC is an integral membrane pigment-protein complex that carries out light-driven electron transfer reactions. One or more electronically excited BChl molecules transfer an electron to nearby acceptor molecules, thereby creating an ion pair state consisting of the oxidized primary donor and a reduced acceptor. After this initial electron transfer event, a series of electron transfer reactions takes place that eventually stabilizes the stored energy in forms that can be used by the cell. The RC complex from the anoxygenic purple bacteria namely

Rhodobacter sphaeroides is the best understood of all photosynthetic RCs, from both a structural and a functional point of view (Deisenhofer & Norris, 1993; Blankenship *et al.*, 1995). These were the first reaction center complexes to be purified and studied by picosecond kinetic methods and the first even to have X-ray structures resolved (Hunter *et al.*, 2008). Much of the molecular level understanding of the early events in photosynthesis is based on the information derived from this system.

1.1.2 Overview of Purple Bacteria

Purple bacteria are photosynthetic gram-negative prokaryotes that convert light energy into chemical energy by the process of anoxygenic photosynthesis. Purple bacteria contain photosynthetic pigments–bacteriochlorophylls and carotenoids—and can grow using inorganic materials as a source of nutrients, with CO_2 as sole carbon source and using photosynthesis or chemosynthesis as a source of energy. Purple sulfur bacteria differ from purple nonsulfur bacteria on both metabolic and genetic basis. The species of two major groups often coexisted under light and anoxic places in nature. Purple sulfur bacteria are poorly equipped for metabolism and growth in the dark, while the purple nonsulfur bacteria possess diverse capacities for dark metabolism and growth. Purple nonsulfur bacteria are a physiologically versatile group of purple bacteria that can grow well both phototrophically and in darkness. Many genera of purple nonsulfur bacteria are known and one of the most widely studied is *Rhodopseudomonas sphaeroides*. This was first identified and named by van Niel (van Niel, 1944). Later this generic name has been changed to *Rhodobacter* (*R.) sphaeroides* and continued to hold the same name (Hunter *et al.*, 2008). These bacteria contain complexes that catalyze light-induced electron and proton transport across the photosynthetic membrane and have been optimized by nature to perform with quantum efficiency close to unity. They grow most rapidly with N_2 as sole nitrogen source and show the highest rates of *in vivo* nitrogenase activity (Madigan, 1984). Purple nonsulfur bacteria occasionally form dense blooms in habitats where levels of sulfide are

either low or undetectable. They are also present in sewage(Holm & Vennes, 1970; Siefert *et al.*, 1978) and waste lagoons (Jones, 1956; Cooper *et al.*, 1975).

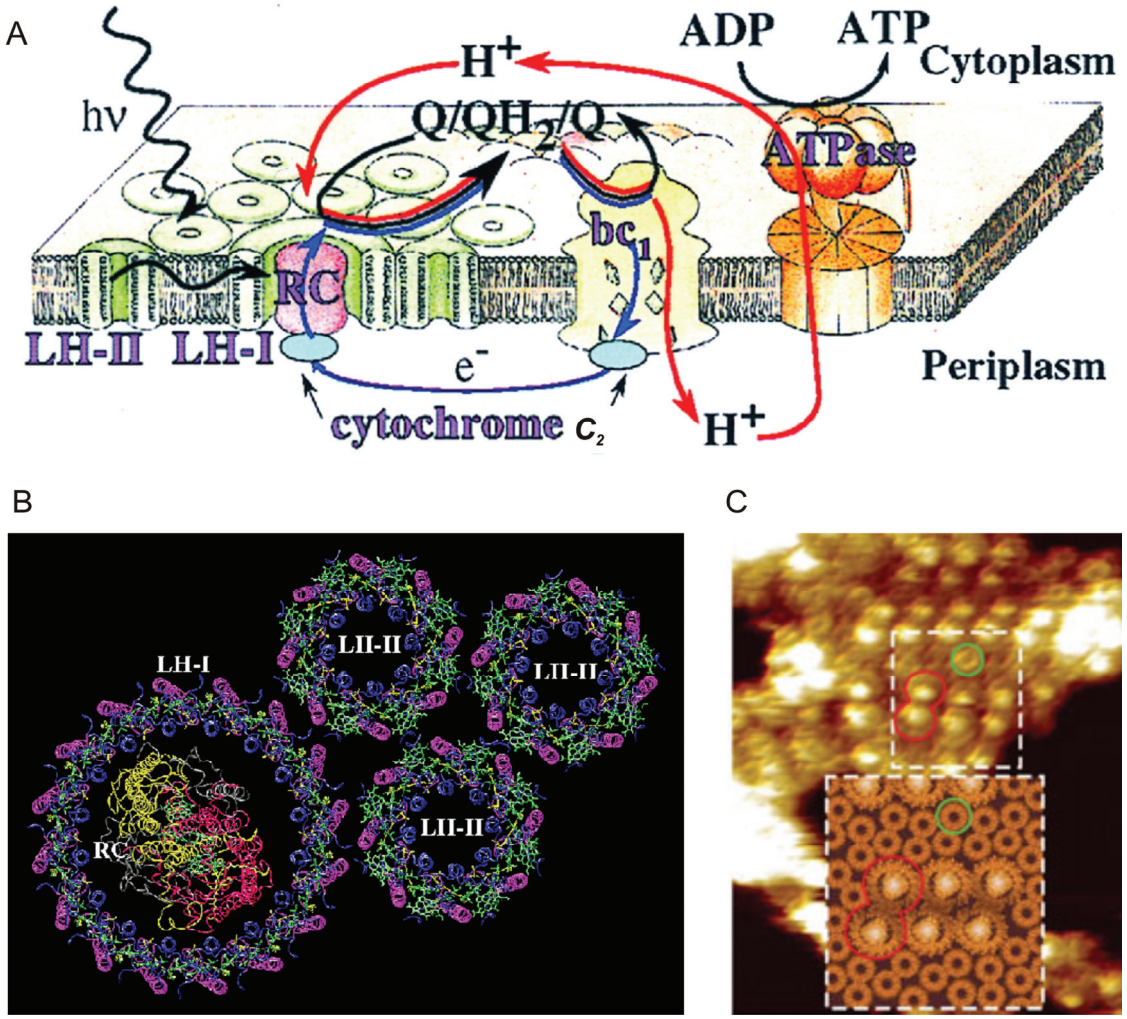

Figure 1.1 (A) Schematic representation of the photosynthetic apparatus in the intracytoplasmic membrane of purple bacteria. The RC (red) is surrounded by the light-harvesting complex I (LH-I, green) to form the LH-I–RC complex, which is surrounded by multiple light-harvesting complexes LH-II (green), forming altogether the PSU. Photons are absorbed by the light-harvesting complexes and excitation is transferred to the RC initiating a charge (electron-hole) separation. The RC binds quinone, reduces it to hydroquinone and releases the latter. This hydroquinone is oxidized by the bc_1 complex, which uses the exothermic reaction to pump protons across the membrane; electrons are shuttled back to the RC by the cytochrome c_2 complex (blue) from the ubiquinone–cytochrome bc_1 complex (yellow). The electron transfer across the membrane produces a large proton gradient that drives the synthesis of ATP from ADP by the ATPase (orange). Electron flow is represented in blue, proton flow in red, and quinone flow, likely confined to the intramembrane space, in black (Hu *et al.*, 1998) Copyright (© 1998) National Academy of Sciences, U.S.A. (B) Arrangement of pigment–protein complexes in the modeled bacterial PSU of *R. sphaeroides*. (Hu *et al.*, 1998) Copyright (© 1998) National Academy of Sciences, U.S.A. (C) AFM picture of photosynthetic membrane, LH2 complexes (green) funnel light energy to RC-LH1 complexes (red) as seen by AFM (small square) or by molecular modeling (bigger square) Reprinted by permission from Macmillan Publishers Ltd: Nature, ref (Bahatyrova *et al.*, 2004) © 2004.

1.1.3 The photosynthetic membrane of purple bacteria

The photosynthetic apparatus of these purple bacteria (Figure 1.1) consists of light harvesting antenna complexes (LH), the RC protein, an ubiquinone-cytochrome *b/c* oxidoreductase complex and ATP synthase (Hu *et al.*, 1998). The energy flow is facilitated by the peripheral light-harvesting complex, LH2, the core light-harvesting complex, LH1 (Karrasch *et al.*, 1995; McDermott *et al.*, 1995; Hu & Schulten, 1998; Bahatyrova *et al.*, 2004) and the RC (Deisenhofer *et al.*, 1985; Allen *et al.*, 1987; Ermler *et al.*, 1994; Camara-Artigas *et al.*, 2002a). The RC reduces quinone to hydroquinone as a result of electron transfer; subsequently the ubiquinol-cytochrome c_2 oxidoreductase (bc_1 complex) (Crofts *et al.*, 1983; Valesco & Crofts, 1991; Gennis *et al.*, 1993; Xia *et al.*, 1997) oxidizes hydroquinone and reduces cytochrome c_2, which completes the cycle by shuttling electrons back to the RC. The ATP-synthase (Junge *et al.*, 1997; Fillingame, 2000; Fillingame *et al.*, 2000) makes use of the resulting proton gradient. The purple bacterial photosynthetic unit displays a certain simplicity in contrast to its counterpart in plants and the supramolecular organization of the constituent proteins is difficult to determine and must be ascertained by combining atomic force microscopy (Bahatyrova *et al.*, 2004; Scheuring *et al.*, 2004; Scheuring & Sturgis, 2005; Scheuring *et al.*, 2005), cryo-electron microscopy (Jungas *et al.*, 1999; Siebert *et al.*, 2004; Qian *et al.*, 2005) and linear dichroism (Frese *et al.*, 2004) studies.

1.1.4 Structure and function of purple bacterial RCs

The structure and function of purple bacterial RCs have been studied over many decades. The crystallographic determination of the RC structure was the first of a membrane protein and has been awarded by the Nobel prize of Chemistry in 1994 to Deisenhofer, Huber and Michel (Deisenhofer *et al.*, 1985).

The RC of *R. sphaeroides* is a transmembrane protein complex made of three major polypeptides, L, M and H (for light, medium and heavy) (Yeates *et al.*, 1987; Ermler *et al.*, 1994; Camara-Artigas *et al.*, 2002a), see Figure 1.2A. The L and M subunits contain five transmembrane α-helices, which are packed together in a

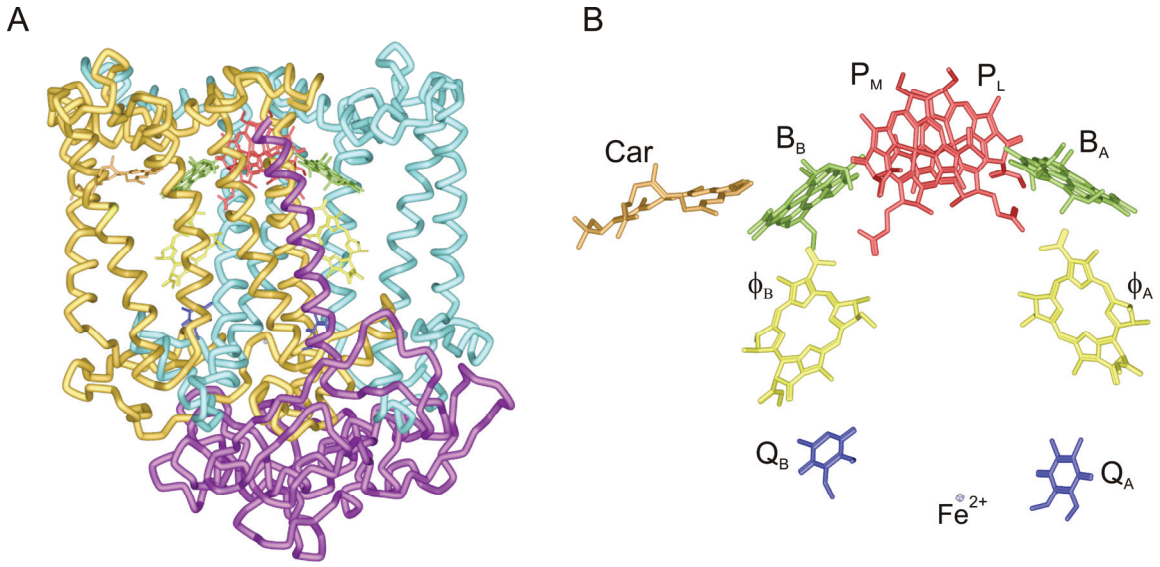

Figure 1.2: (A) The complex arrangement of 3 polypeptide subunits are represented in different colors with a ribbon representation, L (blue), M (yellow) and H (violet) with RC. (B) Clear view of cofactors in the reaction center (RC) of *R. sphaeroides* wild type (WT). The primary electron donor, the special pair, is formed by the two bacteriochlorophyll a (BChl) molecules P_L and P_M. B_A and B_B are accessory BChl cofactors. Φ_A and Φ_B are bacteriopheophytin (BPhe) cofactors. On the acceptor side, two ubiquinone-10 cofactors Q_A and Q_B with a non-heme iron in between are localized. Side chains are omitted for sake of clarity. The symmetry of the cofactor arrangement is broken by a carotenoid cofactor (Car). The light-induced electron transfer occurs selectively via branch A. [PDB entry 1M3X, the figure has been made with Accelrys Discovery Studio] (Camara-Artigas *et al.*, 2002b).

nearly symmetrical way. Subunit H is more globular in shape and is located mainly in the cytoplasmic side of the membrane. The L and M subunits bind the cofactors. Four molecules of bacteriochlorophyll *a* (BChl *a*), two molecules of bacteriopheophytin *a* (BPhe *a*), two ubiquinone-10 molecules (Q), a non-heme iron (Fe^{2+}) and a carotenoid molecule (Car) form the cofactors of the RC protein. The arrangement of the cofactors is shown in Figure 1.2B.

The cofactors form two nearly symmetric branches, the "active" A-branch and the "inactive" B-branch. Two BChls form the primary donor (P), a tightly interacting dimer called the "Special Pair" (P_L and P_M). On either side of the special pair an additional BChl molecule is located, known as the accessory BChl (B_A and B_B). The two BPhe (Φ) are positioned at an edge-to-edge distance of ~14 Å from the special pair.

Situated below the BPhe are the ubiquinones-10, (Q_A and Q_B). Finally, the non-heme Fe^{2+} ion is located in the center of the two branches near the cytoplasmic

side of the membrane. The tenth cofactor, the carotenoid molecule, breaks the apparent symmetry of the cofactor arrangement and is located near B_B. In the RC of *R. sphaeroides* R26, a mutant strain, the carotenoid molecule is not present.

1.1.5 Spectroscopy of RCs

The purple bacterial RC has been studied with many spectroscopic techniques (Hoff & Deisenhofer, 1997). The BChl and BPhe cofactors in particular have distinctive absorbance spectra that provide a very sensitive probe of the structural and functional integrity of the complex, and provide a means to follow the route and rate of light-driven electron transfer.

The absorbance spectrum of the purified *R. sphaeroides* RC is shown in Figure 1.3. Owing to their electronic structure, the BChl and BPhe cofactors give rise to three sets of absorbance bands in the so-called Soret (300–420 nm), Q_x (500–630 nm) and Q_y (650–950 nm) regions. Molar absorption coefficients (ε) for the prominent bands in the Q_y region allow the concentration of RCs to be monitored. A particularly useful feature of the spectrum is that the purity of the complex can be measured from the ratio of protein absorbance at 280 nm to BChl absorbance at 802 nm, with a ratio of 1.3 or less indicating RCs of sufficient purity for crystallization (Okamura *et al.*, 1974). The structural integrity of the RC can be checked through characteristic spectral changes that take place as the protein

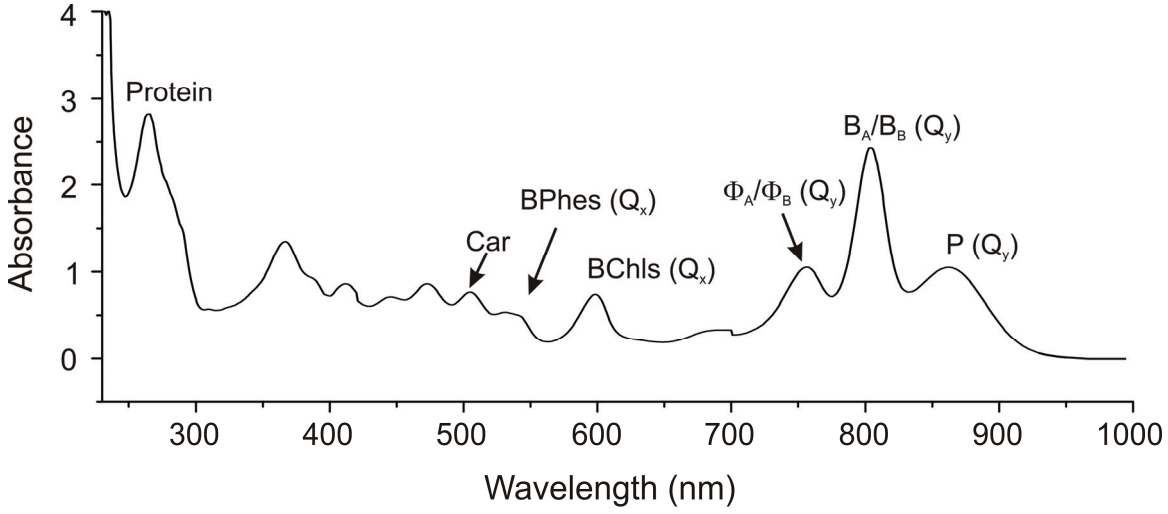

Figure 1.3 The absorbance spectrum of the purified RC of *R. sphaeroides* (WT).

unfolds and the cofactors are released from their native binding sites (Hughes *et al.*, 2006). Photo-oxidation of the RC is accompanied by respective changes in its absorbance spectrum, and especially the Q_y absorbance band attributed to the P BChls at 870 nm vanishes (the term 'bleached' is often used to describe this). The primary donor BChls were first identified through photobleaching of the absorbance band of a BChl species at 870 nm.

1.1.6 Energy and Kinetics of RCs

Though many spectroscopic techniques have been applied, the technique of picosecond-absorbance transient-difference spectroscopy has been very informative with respect to finding the path of the electron flow in these complexes (Blankenship, 2002). Figure 1.4 A and B summarizes the kinetics and energetics of the electron transfer process. After photochemical excitation of P to P*, one electron is transferred to the primary electron acceptor Φ_A within 4 ps, forming the primary radical pair state $P^+\Phi_A^-$ (Martin *et al.*, 1986). The Φ_A^- anion radical decays in about 200 ps and transfers the electron to the ubiquinone Q_A. The

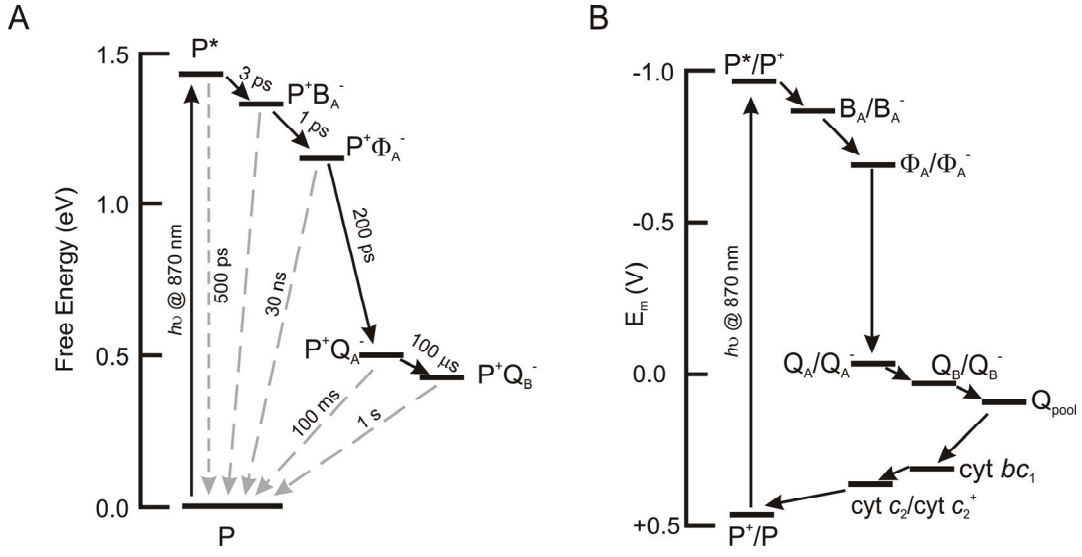

Figure 1.4 (A) Free energies of the states involved in light-activated charge separation in the RCs. (B) Midpoint redox potentials of centres involved in light-driven cyclic electron transfer. Centres are labelled using the convention reactant/product. Cyt bc_1 refers to electron transfer through the high-potential chain formed by the iron–sulfur centre and cytochrome c_1. "This research was originally published in Biochemical Society Transactions. Jones, M. R., The petite purple photosynthetic powerpack. Biochemical Society Transactions. 2009; 37: 400-407 © the Biochemical Society".

electron subsequently moves from Q_A to Q_B in 100 μs reducing Q_B once. Meanwhile, the oxidized primary electron donor P is re-reduced by accepting an electron from cytochrome *c* at the periplasmic side of the protein. The RC can be excited again and Q_A can give a second electron to Q_B. The doubly reduced and protonated Q_B leaves the RC to the ubiquinone pool. New ubiquinone from the ubiquinone pool of the membrane replaces the ubiquinol leading to the initial state of the RC. The movement of charge through the RC proceeds with extremely high quantum efficiency, and at each stage in electron transfer the productive forward reaction (black arrows) is much faster than competing reactions such as recombination of radical pairs to the ground state (grey arrows). To achieve this, movement of the electron through the RC involves the formation of radical pairs with progressively decreased free energies (Figure 1.4B). The P* excited state is a strong reductant, with an estimated excited state redox potential of -940 mV *vs* normal hydrogen electrode (Jones, 2009).

1.1.7 The Solid-state photo-CIDNP effect

The discovery of the solid-state photo-CIDNP effect (for reviews, (Jeschke & Matysik, 2003; Daviso *et al.*, 2008b) by Zysmilich and McDermott in 1994 in frozen and quinone-blocked bacterial RCs of *R. sphaeroides* R26 by ^{15}N magic-angle spinning (MAS) NMR under continuous illumination with white light offered NMR access to the electron-nuclear processes during the charge separation (Zysmilich & McDermott, 1994). By induction of a non-Boltzmann nuclear spin order upon photo-reaction in rigid samples, a signal enhancement of a factor of more than 10,000 has been observed by ^{13}C MAS NMR in several RCs (Prakash *et al.*, 2005; Prakash *et al.*, 2006). In the meantime, the solid-state photo-CIDNP has been observed also on *Rhodopseudomonas acidophila* (Diller *et al.*, 2008) of the green sulphur bacterium *Chlorobium tepidum*, (Roy *et al.*, 2007) of the heliobacterium *Heliobacillus mobilis* (Roy *et al.*, 2008) as well as of the photosystems I and II of plants (Matysik *et al.*, 2000a; Alia *et al.*, 2004; Diller *et al.*, 2007b) and algae (Janssen *et al.*, 2010). The signal enhancement provided by the solid-state photo-CIDNP

effect may thus be considered an intrinsic property of natural photosynthetic RCs and allows directly resolving the signals of ^{13}C atoms within the RC (Matysik *et al.*, 2009).

Under continuous illumination on RCs of *R. sphaeroides* WT, two solid-state mechanisms run in parallel to induce net nuclear polarization which remains under steady-state conditions (Jeschke & Matysik, 2003; Daviso *et al.*, 2008b): (i) Electron–electron–nuclear three-spin mixing (TSM) breaks the balance by coherent evolution of the correlated radical pair state in interaction with the nuclear spins and the applied magnetic field, depending on the signs of the electron–electron and of the anisotropic electron–nuclear interactions (Jeschke, 1997, 1998). (ii) In the electron-nuclear differential decay (DD) mechanism (Polenova & McDermott, 1999) only a single matching condition with a dependence of secular part of the hyperfine coupling is required and the difference of singlet and triplet radical pair lifetimes must be of the order of the inverse hyperfine coupling (Jeschke & Matysik, 2003). The mechanism has been summarized and explained in Chapter 2 (this thesis). Understanding of the spin-chemical processes (Daviso *et al.*, 2009a) allowed to apply photo-CIDNP MAS NMR as an analytical tool for elucidating electronic structures of the cofactors forming radical pairs (Daviso *et al.*, 2009c).

1.2 Theoretical background of Solid State NMR

1.2.1 Basic interactions in solid state NMR

Nuclear magnetic resonance (NMR) has established its own importance starting from structural characterization of liquids, compounds in solution and solids, further to polymers, proteins and also membrane proteins (Schmidt-Rohr & Spiess, 1994). The advances in multidimensional NMR have been exploited in many fields in physics, chemistry, material science and also in biology.

Lorentz predicted the splitting of spectral lines of an atom placed in an external magnetic field on the basis of classical theory. This splitting was first observed by Zeeman. The Zeeman interaction in NMR describes the interaction

between the nuclear magnetic moment (μ) of a spin with an external static magnetic field B_0 in the spin Hamiltonian, and is expressed as

$$H_0 = -\mu \cdot B_0 . \qquad 1.1$$

The magnetic moment (μ) can be expressed in terms of a nuclear spin operator I as $\mu = \gamma\hbar I$, and equation 1.1 can be rewritten as

$$H_0 = -\gamma\hbar I_z B_0 \qquad 1.2$$

assuming that B_0 points in the Z-direction. Although the Zeeman interaction is the most dominant interaction in NMR and generally determines the quantization z-axis of the spins, it contains little structural information in itself (Abragam, 1961).

In NMR, relevant chemical and structural information originates from the local fields that the nuclear spins experience. These fields are due to the shielding of the B_0 field by the electron clouds and from all the interactions between the spins. For an ensemble of nuclear spins placed in a large magnetic field containing two types of nuclei, *i.e.* abundant spins *I* (e.g., ^{1}H) with a gyromagnetic ratio γ^I and a resonant frequency of ω_I and a rare spin *S* (e.g., ^{13}C, ^{15}N) with a gyromagnetic ratio of γ^S and a resonance frequency of ω_S, the interactions can be described in the spin Hamiltonians by the chemical shift term H_{CS}, and the homonuclear and heteronuclear dipolar terms, H_D^{II} and H_D^{IS} respectively. In the lab frame all the interactions can be represented by the spin Hamiltonian

$$H = H_0 + H_{CS} + H_D^{II} + H_D^{IS} . \qquad 1.3$$

1.2.2 Chemical shielding Hamiltonian

The chemical shielding Hamiltonian describing the electron distribution acting on a spin *I*, is expressed by

$$H_{CS} = -\gamma\sigma_{zz} I_z B_0 , \qquad 1.4$$

where $\sigma_{pq}(p,q = x,y,z)$ are the components of chemical shielding tensor, in the laboratory frame where the z axis is along the static magnetic field.

The electronic distribution around a nucleus in a molecule is rarely spherically symmetric. Since the chemical shielding arises from the electronic surroundings of a nucleus, its value depends on the orientation of the molecule in the magnetic field B_0. This orientation dependence is best described in terms of a chemical shielding tensor, which is a 3×3 matrix with elements σ_{pq} determined by the orientation of the laboratory frame with respect to a molecular principle axes frame where $\sigma_{PQ} = 0$ for $P \neq Q$ and by σ_{XX}, σ_{YY} and σ_{ZZ} themselves.

In solid-state NMR, the three principal axis tensor elements are often replaced by

$$\sigma_{iso} = \frac{1}{3}\left(\sigma_{XX} + \sigma_{YY} + \sigma_{ZZ}\right), \qquad 1.5$$

$$\delta = \sigma_{ZZ} - \sigma_{iso}, \qquad 1.6$$

$$\eta = \frac{\sigma_{XX} - \sigma_{YY}}{\delta} \qquad 1.7$$

Here, σ_{iso} is the isotropic value, while δ and η are the chemical shift anisotropy (CSA) and asymmetry parameter, respectively (Schmidt-Rohr & Spiess, 1994; Duer, 2004).

The expression for the anisotropic frequency shift of a single site in a static sample can be derived from the values δ, η and the polar angles (θ,ϕ) of the B_0 field in the principal axis system

$$\omega(\theta,\phi) = \frac{1}{2}\delta(3\cos^2\theta - 1 - \eta\sin^2\theta\cos(2\phi))\gamma B_0 . \qquad 1.8$$

And the chemical shielding Hamiltonian H_{CS} in the principal axis system becomes

$$H_{\mathrm{CS}} = \{\sigma_{\mathrm{iso}} + \frac{1}{2}\delta[3\cos^2\theta - 1 - \eta\sin^2\theta\cos(2\phi)]\}\gamma B_0 I_z . \qquad 1.9$$

1.2.3 Dipolar coupling Hamiltonian

The heteronuclear coupling is responsible for much of the broadening observed in the solid-state NMR spectrum. Since each spin represents a nuclear magnetic moment that produces a small magnetic field, every spin "feels" the magnetic field

produced by the nearby spins. The strength of the heteronuclear dipolar coupling is represented by the truncated dipolar Hamiltonian

$$H_{\mathrm{D}}^{IS} = -\frac{\mu_0}{4\pi}\hbar\sum_i\sum_j \frac{\gamma^I\gamma^S}{r_{ij}^3}\frac{1}{2}(3\cos^2\theta_{ij}-1)2I_z^iS_z^j, \qquad 1.10$$

where r_{ij} represents the internuclear distance, μ_0 is the vacuum permeability, γ^I and γ^S are the gyromagnetic ratios of the interacting *I* and *S* spins, respectively, and I_z^i and S_z^j are the z-components of the nuclear spin angular momentum operators respectively. The angle θ_{ij} describes the orientation of the internuclear vector with respect to the orientation of the external magnetic field. Since the magnitude of the coupling between two nuclear spins has a r^{-3} distance dependence, the dipolar coupling is a long-range through space interaction. Spins also experience a homonuclear dipolar coupling, which results from an interaction between spins of the same species. The homonuclear dipolar Hamiltonian of the *I* spins is given by

$$H_{\mathrm{D}}^{II} = -\frac{\mu_0}{4\pi}\hbar\sum_i\sum_j \frac{\gamma^{\mathrm{I}}\cdot\gamma^{\mathrm{I}}}{r_{ij}^3}\frac{1}{2}(3\cos^2\theta_{ij}-1)(3I_z^iI_z^j-\mathbf{I}^i\cdot\mathbf{I}^j). \qquad 1.11$$

There again r_{ij} and θ_{ij} represent the internuclear distance and the angle between this internuclear vector and the external magnetic field, respectively. Two equivalent spins are able to undergo an energy-conserving "flip-flop" transition in which one spin flips up while the other spin flips down (Schmidt-Rohr & Spiess, 1994).

1.3 High resolution NMR Techniques for solids

In liquid-state NMR, spectra consist of a series often resolved lines that are due to the averaging of the anisotropic NMR interactions by rapid tumbling of the molecules. In contrast, in solid-state NMR the effects of anisotropic interactions are observed and hence the resulting signals are generally very broad. Therefore special techniques for coherent averaging of the couplings "in spin space" and "in real space" by sample rotations and pulse sequence are essential for high resolution solid state NMR spectra (Schmidt-Rohr & Spiess, 1994).

1.3.1 Magic angle spinning

Magic-angle spinning (MAS) is routinely used in the majority of solid-state NMR experiments. As discussed in earlier sections 1.2.2 and 1.2.3, the dependence on the molecular interaction is of the form $\left(3\cos^2\theta - 1 - \eta\sin^2\theta\cos(2\phi)\right)$, where the angle (θ,ϕ) describes the orientation of the interacting tensors, in particular the chemical shielding and dipolar coupling $(\eta = 0)$ tensors. In the MAS experiment, the sample is spun rapidly in a cylindrical rotor around a spinning axis oriented at the magic angle $\left(\theta_m = \arccos\left(1/\sqrt{3}\right) = 54.74^0\right)$ with respect to the applied magnetic field B_0 (Andrew *et al.*, 1958; Lowe, 1959). MAS makes the average of the heteronucelar dipolar coupling and CSA interactions zero. Thus at fast sample rotation, the inhomogeneous anisotropic line broadenings are removed resulting in narrow central lines flawed by narrow sidebands. The spinning also partially removes homonuclear dipolar-coupling effects. For a detailed mathematical description of MAS, see (Duer, 2004).

1.3.2 Cross-polarization

Cross-polarization (CP) is the most important signal enhancement technique in solid-state NMR. It was introduced in 1962 by Hartmann and Hahn for static samples. Here nuclear polarization is transferred from abundant spins (I = ^{1}H) to rare spins (S = ^{13}C, ^{15}N) relying on the heteronuclear dipolar interaction (Figure 1.5). The maximum possible enhancement factor for the signals of the rare spins is given by γ_I / γ_S, which is 4 for ^{1}H and ^{13}C (Schmidt-Rohr & Spiess, 1994). The

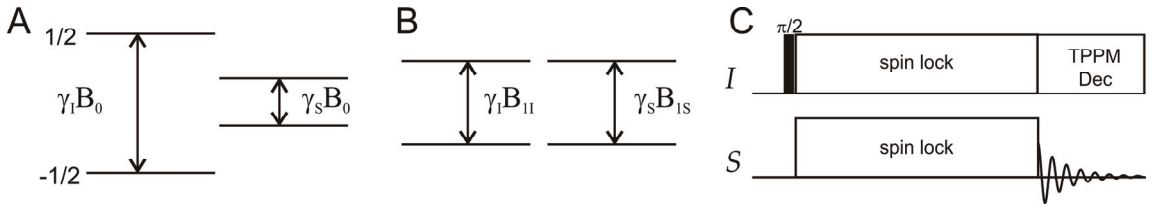

Figure 1.5 Energy levels of the I (^{1}H) and S (^{13}C) spins. (A) In the laboratory frame the transfer of magnetization is not possible. (B) In the rotating frame the transfer of magnetization is possible as the energy separation is determined by the rf-field. The matching condition is then fulfilled. (C) Pulse sequence for HH-CP.

transfer can be described in the doubly rotating frame, that is, one in which the ^{1}H spins are considered in a frame in which all the rf irradiation fields during ^{1}H pulses appear static, and the *S* spins are considered in a frame in which all the rf fields appear static. Here we assume that all pulses are exactly on resonance for the spins to which they are applied. The simple pulse sequence is shown in Figure 1.5B. An initial $\pi/2$ pulse is applied on the *I* spins and the resulting magnetization is locked at an rf field B_{1I}. Simultaneously another spin-lock field of B_{1S} is applied to the *S* spins that has the same nutation frequency $\omega_{1S} = \gamma_S B_{1S}$ as the one on the *I* spins $\omega_{1I} = \gamma_I B_{1S}$, thus satisfying the Hartmann-Hahn (HH) condition (Hartmann & Hahn, 1962)

$$\omega_{1I} = \omega_{1S} . \qquad 1.12$$

The transfer depends on how well the HH condition is fulfilled. Typical rf-field strengths for the HH CP are between 50 kHz and 100 kHz. The optimal CP contact time depends on the size of the heteronuclear dipolar coupling and on rotating frame relaxation times $T_{1\rho}$ of the two spins.

Advantages of the CP over the direct excitation of low abundant spins are the increase in polarization and faster repetition delays due to shorter relaxation times of abundant spins. CP can be combined with MAS leading to modified HH matching conditions

$$\pm\left(\omega_{1I} - \omega_{1S}\right) = n\omega_r . \qquad 1.13$$

Here the difference between the rf-field amplitudes must be an integral multiple of the spinning frequency (Stejskal *et al.*, 1977; Stejskal *et al.*, 1984).

1.3.3 Spin decoupling

Although MAS removes the main effects of the anisotropic dipolar interactions on the linewidths, higher order effects must be still removed by spin decoupling. This can be achieved through the application of rf-frequency irradiation schemes on the non-observed spins for heteronuclear interactions and on the observed spins for homonuclear interactions. There are several techniques either for heteronuclear decoupling, such as CW and gated decoupling, TPPM, SPINAL, XiX, SW$_f$-TPPM

or for homonuclear decoupling such as LG, WAHUHA, MREV-8, BR-24, FSLG, PMLG, DUMBO etc. A few of the mentioned techniques are discussed below.

1.3.3.1 Continuous wave (CW) decoupling

For a spin system, where a single spin *S* is coupled to a number N of *I* spins, continuous high power rf-field irradiation on the *I* spins eliminates the effect of the heteronucelar couplings on the observed *S* spin, regardless of the states of its magnetization (Sarles & Cotts, 1958).

1.3.3.2 Two-pulse phase modulated decoupling (TPPM)

TPPM was the first multiple-pulse decoupling sequence (Bennett *et al.*, 1995) which improved heteronuclear decoupling efficiency compared to CW decoupling. This sequence consists of a continuous repetition of two pulses of length τ_p and phase $\pm\phi$. The phase and the angle of the pulses are 15^0 and 180^0, but in practice the exact phase and length values are best optimized experimentally. At slow spinning speeds, the variation of these values of efficient decoupling is quite large, but at high MAS frequencies, the sequence needs to be optimized very carefully in order to obtain narrow lines.

1.3.3.3 Lee-Goldburg (LG) decoupling

MAS can be used to remove the effects of the homonuclear dipolar couplings on NMR spectra, provided the spinning frequency is much faster than the strength of the dipolar interactions, which for protons are usually of the order of tens of kHz. Thus spinning frequencies up to 70 kHz are not sufficient to decouple and multiple-pulse sequences must be applied to suppress the homonuclear dipolar line-broadening effects. The Lee-Goldburg scheme is shown in Figure 1.6. The basic principle of this technique is to irradiate the protons continuously with an off-resonance rf-field of intensity $\omega_1 = -\gamma B_1$ and off resonance value $\Delta\omega_{LG} = \omega_{rf} - \omega_0$, in such a way that the total effective field B_{eff} in the rotating frame is inclined at the magic angle $\theta_m = 54.74^0$ with respect to the static magnetic

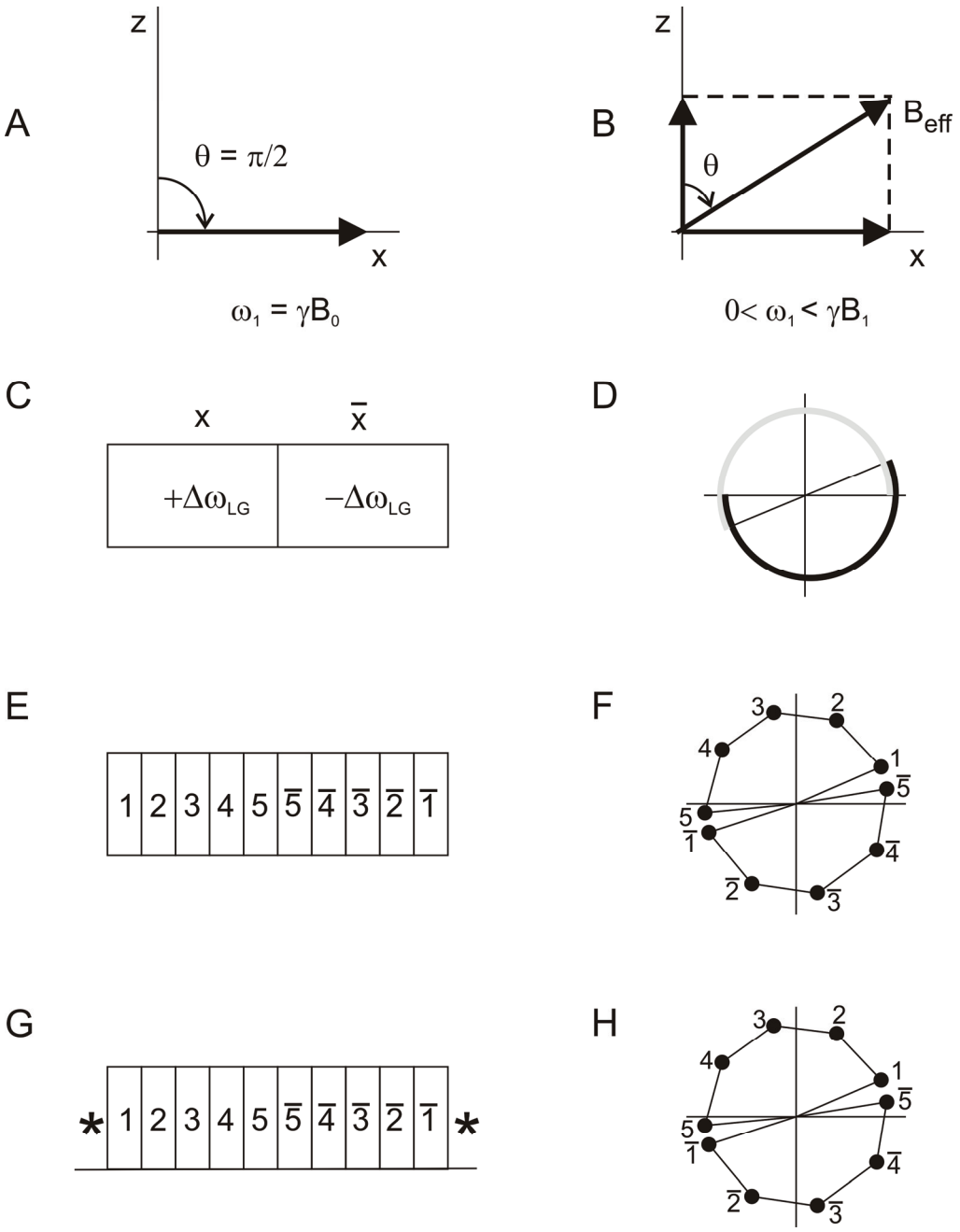

Figure 1.6 The Lee-Goldburg scheme, viewed from rotating frame, where $\omega_{frame} = -\omega_{RF}$ around the z-axis. (A) on-resonance, (B) off-resonance with rf-fields. The pulse schemes and time dependent rf irradiation field profiles in the xy-plane of the on-resonance rotating frame of FSLG (C, D), PMLG5 (E, F) and *w*PMLG5 (G, H). Asterisks denote possible data sampling points. The rotation frequencies ΔLG (grey) and −ΔLG (black) of the irradiation vector in the case of FSLG obey the relation ΔLG = $\omega_1/\sqrt{2}$, where ω_1 is the rf intensity. The continuous time-dependent phase in FSLG is replaced in PMLGn by n discrete phases (shown by dots in E – H). The set of phase values for both PMLG5 and for *w*PMLG5 are given below

$$\phi_1 = 20.78^0, \phi_2 = 62.34^0, \phi_3 = 103.9^0, \phi_4 = 145.46^0, \phi_5 = 187.02^0, \phi_{\bar{5}} = 7.02^0, \phi_{\bar{4}} = 325.46^0,$$
$$\phi_{\bar{3}} = 283.9^0, \phi_{\bar{2}} = 242.34^0, \phi_{\bar{1}} = 200.78^0$$

field direction. The LG condition is given by

$$\pm \Delta\omega_{LG} = \pm \frac{1}{2}\sqrt{2}|\omega_1| \qquad 1.14$$

(Lee & Goldburg, 1965).

The LG irradiation scheme averages the homonuclear dipolar interaction to zero-order, and a scheme can be incorporated with standard HH-CP to suppress the proton-proton interactions during the CP transfer experiment. This is referred to as LG-CP. Several variations and modifications of the LG scheme, to improve the averaging of spin-space interactions are in use. For example: (i) Frequency-switched LG (FSLG): This involves application of an off-resonance rf-field at $+\Delta\omega_{LG}$ for a duration of τ_{LG} with phase x, immediately followed by the application of another off-resonance rf-field at $-\Delta\omega_{LG}$ for a duration of τ_{LG} with phase $\bar{x}$ (Mehring & Waugh, 1972; Bielecki *et al.*, 1989; Levitt *et al.*, 1993). This involves simultaneous switching of both the phase and the frequency of the rf-irradiation as shown in Figure 1.6 (C & D). (ii) Phase-modulated LG (PMLG): This consists of a series of pulses in which the phase is changed, while their frequencies are kept constant. Hence, in both FSLG and PMLG, both the zero- and the first-order homonuclear dipolar interactions are averaged. A PMLG*n* cycle approximates an LG unit by *n* on-resonance pulses, each with duration of τ_{LG}/n, with n= 3,5,9… and a phase increment of $\Delta\Phi = 207.8/n$ between successive pulses, again followed by the same set of pulses in the reverse order with an overall phase shift of 180^0 with respect to the first set. The pulse sequence and the rf profile in the on-resonance rotating frame are shown in Figure 1.6 (E & F). High-resolution ^{1}H spectra can then be obtained in a 1D way by inserting observation windows in the PMLG cycle, *w*PMLG*n* (Vinogradov *et al.*, 2002). The rf-schematic of this approach is shown in Figure 1.6 (G & H) (Vinogradov *et al.*, 2005). Implementing such sequences is experimentally challenging since the free-induction decay (FID) data points are collected at particular points in between sets cycle of pulses. High power with short pulse lengths is required to achieve maximum decoupling efficiency.

1.3.4 Recoupling techniques

Fast MAS averages the inhomogeneous and partly the homogeneous anisotropic interactions present in the solid-state, giving rise to narrow lines in the spectra. As a result, the structural information about the distance and orientation content of these interactions is lost. Using recoupling techniques, it is possible to reintroduce homonuclear and heteronuclear dipolar couplings even under MAS conditions. Recoupling reintroduces the anisotropic interactions under MAS by interfering with the averaging of the spatial part through manipulations of the spin part. Such techniques are based on the fact that the dipole-dipole coupling between nuclei that are spatially close permits the build-up of zero-quantum or double-quantum coherences. These can be classified into heteronuclear and homonuclear recoupling sequences.

1.3.4.1 Heteronuclear recoupling sequence

CP and phase- or frequency- switched LG-CP under MAS conditions are examples for heteronuclear recoupling of dipolar interactions. Examples of other well known solid-state NMR recoupling techniques are R3, REDOR and TEDOR (Oas *et al.*, 1988; Gullion & Schaefer, 1989; Hing *et al.*, 1992). In particular we should mention that the symmetry theory of recoupling (Levitt, 2002) has facilitated the plan of designing rotor-synchronized radio-frequency pulse sequences which selectively restore subsets of spin interactions, and suppress others (Eden & Levitt, 1999; Carravetta *et al.*, 2000; Brinkmann & Levitt, 2001).

1.3.4.2 Homonuclear recoupling sequences

A number of sequences for broadband ^{13}C–^{13}C dipolar recoupling under MAS conditions have been developed, such as PDSD, RFDR and DARR (Szeverenyi *et al.*, 1982; Bennett *et al.*, 1992; Takegoshi *et al.*, 2001). PDSD (Proton-Driven Spin Diffusion) was one of the first experiments used for dipolar-mediated polarization transfer under MAS. The transfer of magnetization from ^{13}C to ^{13}C occurs directly through space and is mediated by the interaction with the protons. The polarization transfer is inefficient when the ^{13}C-^{13}C dipolar coupling is smaller

than the difference of their resonance frequencies. Since no rf radiation is applied during the PDSD mixing time in 2D experiments, the recoupling is most efficient at low spinning frequencies. Typical mixing times in protonated compounds are in the order of 10 ms for ^{13}C-^{13}C transfer via direct bonds up to several 100 ms for long range transfer (Szeverenyi *et al.*, 1982; Grommek *et al.*, 2006). However, in such long-range transfers, the ^{13}C-^{13}C correlations tend to be lost due to the so-called dipolar truncation effect. The strong dipolar coupling for a pair of adjacent ^{13}C–^{13}C spins tends to suppress weaker couplings between a ^{13}C spin in the pair and remote ^{13}C spins (Baldus & Meier, 1997; Hoshino *et al.*, 1998; Hohwy *et al.*, 1999).

In DARR (^{13}C–^{1}H dipolar-assisted rotational resonance), broadband recoupling is achieved by ^{13}C–^{13}C spectral overlap, made possible by ^{13}C-^{1}H interactions. The ^{13}C–^{1}H dipolar interaction is recovered by suitable rf irradiation on the protons. This sequence recouples ^{13}C–^{13}C dipolar interactions broadbandly but non-uniformly. This unique feature makes it possible to suppress the dipolar truncation effects even though the sample is extensively ^{13}C labeled (Takegoshi *et al.*, 2001; Takegoshi & Terao, 2002; Crocker *et al.*, 2004).

1.3.5 Spin diffusion

The term "spin diffusion" was first introduced by Bloembergen to describe the phenomenon of polarization transfer through homonuclear dipolar couplings in solids which on a macroscopic level looked like a diffusion process (Bloembergen, 1949). In general, spin diffusion can be observed on two different physical scales, either as spatial spin diffusion or as spectral spin diffusion. Spatial spin diffusion describes the flow of magnetization in space between equivalent nuclei due to a non-equilibrium distribution of the initial longitudinal magnetization (Abragam, 1961). Spectral spin diffusion is the flow of polarization between spins of different resonance frequencies (Suter & Ernst, 1982). Real systems often show both aspects of spin diffusion. Spin diffusion has two important application aspects in solid-state NMR namely, (i) as a transport mechanism to transfer magnetization in a

two-dimensional correlation experiment which then establishes the relative orientation of tensorial interactions (Linder *et al.*, 1985) and (ii) measuring distances between spins, e.g., between domains in a heterogeneous polymer (Cheung, 1981; Heinen *et al.*, 1998; Mulder *et al.*, 2000).

Spin diffusion between protons can be used to measure domain sizes in polymers. Usually, these systems have a dense network of homonuclear dipolar couplings resulting in a fast spin-diffusion rate constant. Here, the diffusion rate constants are in the order of about 1 nm^2/ms, allowing to probe distances up to 200 nm (Schmidt-Rohr & Spiess, 1994). Such true ^1H spin diffusion has revealed long-range inter-molecular distance restraints in a self-aggregated Chl *a* samples (de Boer *et al.*, 2002). Recently, similar experiments have been applied to chlorosomes to determine the orientation of BChls (Ganapathy *et al.*, 2009).

Proton-driven spin diffusion between rare nuclei is a "classical" spin diffusion experiment applied to obtain distance constraints. Biosynthetically site-directed, ^{13}C and ^{15}N labelled samples allowed the observation of long-range distance correlations up to 7Å in the α-spectrin SH3 domain (Castellani *et al.*, 2002). Such spin diffusion experiments also allow the observation of polarization transfer across small couplings even in the presence of strong coupling without severe dipolar-truncation effects (Grommek *et al.*, 2006). Recently, complex formation and light activation in membrane-embedded sensory rhodopsin II has been observed by such experiments (Etzkorn *et al.*, 2010).

1.4 Aim and scope of this thesis

Light-induced charge transfer in photosynthetic RCs is highly efficient, having a quantum yield for the entire electron transfer chain close to unity. Artificial systems have not yet reached such yield, and it is not clear how to improve their efficiency. In RCs of *R. sphaeroides*, the electron transfer is selective on one of the two symmetric branches of cofactors. It is observed that electron transfer in structurally similar RCs, as that of photosystem I, occurs equally over both branches, to make the mechanism of charge separation even more mysterious. To solve these questions, the first goal to reach will be to construct a complete picture

of the orbitals involved in electron transfer. A second goal is to complement such a static orbital picture with dynamic information. Since electron transfer is coupled to phonons, it is related to local mobility, which might be crucial for directing the transfer and for dissipating efficiently the energy. A third aspect is to which degree and by what means the environment of the protein tunes the properties of the entire electron transfer pathway.

The solid-state photo-CIDNP effect with its dramatic enhancement of local NMR signals provides an analytical tool that is especially suited for studying electron transfer in photosynthetic RCs. In fact, photo-CIDNP MAS NMR has been applied to explore the electronic structures of the electron donors. It was possible to obtain an almost complete picture of the electronic ground state of the donor in the mutant *R. sphaeroides* R26 (Daviso *et al.*, 2009c). Also other donors have been analyzed, for example the donor of photosystem II of plants, which has been identified to be monomeric and highly asymmetric (Matysik *et al.*, 2000a; Diller *et al.*, 2007b). In this thesis, the photo-CIDNP MAS NMR assessment of electronic structure of the donor of *R. sphaeroides* WT, the Special Pair in its ground state will be completed (**Chapter 2**). In addition, the electronic structure of the acceptor, the bacteriopheophytin, will be provided (**Chapter 4**).

For studying the dynamics of the Special Pair, a new strategy is introduced, aiming to further develop the methodology of photo-CIDNP MAS NMR. A spin-torch type experiment is applied here by transferring the photo-CIDNP polarization to nearby carbon atoms by using ^{13}C-^{13}C spin diffusion between different isotope labels. Thus, local mobility will be probed (**Chapter 3**).

To explore the protein pocket, which might tune to the Special Pair, an alternate spin-torch experiment using protons is proposed. In this concept, the strong polarization of the donor carbons is transferred to the pocket, which can be studied at atomic resolution. To this end, the possibility to use ^{13}C photo-CIDNP for ^{13}C-^{1}H transfer is explored (**Chapter 5**).